

A simple method to construct eigenset of single-active-electron atom in momentum space with applications to solve time-dependent Schrödinger equation

Shih-Da Jheng and Tsin-Fu Jiang*

Institute of Physics, National Chiao Tung University, Hsinchu 30010, Taiwan

(Dated: June 1, 2021)

Abstract

We present a highly accurate method for solving single-active-electron (SAE) atomic eigenset in momentum space. The trouble of Coulomb kernel singularity is bypassed with numerical quadrature, which is simple but effective. The complicated Lande regularization method is no longer necessary. The data of accuracy for some low-lying states of the hydrogen and SAE helium atom were tabulated. Two examples of using the generated eigenset to solve the hydrogen atom under strong-field laser pulses were shown. The momentum and the coordinate representation are complementary to each other in quantum mechanics. The simple method to generate eigenstates and the localized behavior of wave functions in momentum space would be useful in the study of quantum mechanical problems involving continuous states.

PACS numbers: 2.70.Hm,31.15.B-,31.15.X-,02.60.Cb

* tfjiang@nctu.edu.tw

I. INTRODUCTION

The continuous eigenstates of a Schrödinger equation usually spread over a large volume in coordinate space (R -space). From the complementary principle of quantum mechanics, the corresponding momentum space (P -space) volume will be finite and small for continuous states. Hence, solving quantum mechanical problems in momentum representation have the numerical advantage, especially for wide-spreading states in R -space [1, 2]. Although we can easily calculate low-lying bound states with modest grids and finite range in R -space, but for problems involved continuous states, special efforts are required. Some sophisticated methods can be found in [3–5]. In the early years, Podolanski and Pauling [6] calculated the Fourier transform of the hydrogen R -space bound states into P -space. Fock recognized the hydrogen bound solution is a 3-dimensional sphere embedded in a 4-dimensional space [7]. He found that the discrete spectrum in P -space is the Riemann geometry with constant positive curvature, and the continuous spectrum is the Lobachevskii geometry with the constant negative curvature [8]. For practical applications in P -space, there is a singularity in the Coulomb kernel of the integral eigenvalue equation which causes numerical trouble [9–11]. Lande discovered a subtraction method to regularize the singularity [12]. The Lande method was adopted in several subsequent applications [1, 13, 14]. Recently, we improved the Lande subtraction method by using a reasonable small momentum upper limit instead of mathematical infinity. The accuracy and efficiency are both significantly enhanced. We showed that the time-dependent Schrödinger equation (TDSE) of a hydrogen atom under irradiating of intense laser pulse can be calculated by using the generated P -space eigenset of the hydrogen atom. The photoelectron spectra and high-order harmonic generations were obtained without cooperating to other approximations [15].

However, the Lande regularization method has never been straightforward in coding, and application was limited. A simpler formalism than the Lande subtraction method will be useful for working in momentum space. In this paper, we developed a simple but highly accurate method to construct the numerically complete eigenset of SAE atom in momentum space. The singularity in P -space Coulomb kernel can be bypassed with numerical quadrature. The SAE eigenset can then be solved easily. The accuracies of energy levels and standard deviations of wave functions are both much improved compared with the Lande method. The development may facilitate the momentum space applications in quantum

mechanical problems. Next, in Sec.II, the formalism was outlined. In Sec.III, the results and accuracy of hydrogen and SAE helium were presented. In Sec. IV, we showed two calculations of a hydrogen atom under strong-field laser pulse with the eigenset and compared to published results to demonstrate the usage of our method. This is followed by conclusions in Sec. V. Atomic units ($m_e = e = \hbar = 1$) are used throughout this paper.

II. METHOD OF SAE EIGENSTATE CALCULATION

In the single-active electron model potential for atoms [16], the effective potential contains the nuclear Coulomb potential $-Z/r$, and the short-ranged potential $V_{short}(r)$ from the screening of other electrons. Let an eigenstate be written as

$$\Phi_{nlm}(\vec{p}) = \frac{\chi_{nl}(p)}{p} Y_{lm}(\Omega_p),$$

then we have [9–11]

$$\left[\frac{p^2}{2} - E\right]\Phi(\vec{p}) + \int W(\vec{p} - \vec{q})\Phi(\vec{q})d^3q = 0. \quad (1)$$

Where we have defined

$$\begin{aligned} \Phi(\vec{p}) &= 1/(2\pi)^{\frac{3}{2}} \int \Psi(\vec{r})e^{-i\vec{p}\cdot\vec{r}}d^3r, \\ W(\vec{Q}) &= 1/(8\pi^3) \int_{r=0}^{r=R_m} r^2 dr \int d\Omega_r \left[\frac{-Z}{r} + V_{short}(\vec{r})\right]e^{-i\vec{Q}\cdot\vec{r}}, \end{aligned} \quad (2)$$

with $\vec{Q} = \vec{p} - \vec{q}$. Instead of $r \in (0, \infty)$ in radial integration mathematically, we numerically integrate it up to a large enough upper limit R_m where the short-ranged potential vanished. For the SAE atomic potential, we use

$$V_{short}(r) = -\frac{a_1e^{-a_2r} + a_3re^{-a_4r} + a_5e^{-a_6r}}{r}, \quad (3)$$

with parameters $a_1 = 1.231, a_2 = 0.662, a_3 = -1.325, a_4 = 1.236, a_5 = -0.231, a_6 = 0.480$ for helium atom [16]. The energy levels were calibrated to NIST database [17]. We obtain

$$W(\vec{Q}) = W_{Coul}(\vec{Q}) + W_{short}(\vec{Q}), \quad (4)$$

$$W_{Coul}(\vec{Q}) = \frac{Z}{2\pi^2} \frac{\cos(QR_m) - 1}{Q^2}, \quad (5)$$

$$W_{short}(\vec{Q}) = \frac{-1}{2\pi^2} \left\{ \frac{a_1}{a_2^2 + Q^2} + \frac{2a_3a_4}{(a_4^2 + Q^2)^2} + \frac{a_5}{a_6^2 + Q^2} \right\}. \quad (6)$$

The kernel $W(\vec{p} - \vec{q})$ depends only on p, q and the angle θ between \vec{p} and \vec{q} . We can make the expansions :

$$W_{Coul}(\vec{p} - \vec{q}) = \sum_{l=0}^{\infty} (2l+1) a_l(p, q) P_l(\xi), \quad (7)$$

$$W_{short}(\vec{p} - \vec{q}) = \sum_{l=0}^{\infty} (2l+1) b_l(p, q) P_l(\xi), \quad (8)$$

where $\xi = \cos \theta$, and $P_l(\xi)$ is the Legendre polynomial of order l . Let $z = \frac{p^2+q^2}{2pq} \geq 1$, then

$$a_l(p, q) = \frac{Z}{8\pi^2 pq} \int_{-1}^1 d\xi \frac{P_l(\xi)}{z - \xi} [\cos(\sqrt{2pq(z - \xi)} R_m) - 1], \quad (9)$$

$$b_l(p, q) = \frac{1}{2} \int_{-1}^1 d\xi P_l(\xi) W_{short}(\vec{p} - \vec{q}). \quad (10)$$

The known Coulomb singularity occurs when $\vec{Q} = 0$, that is, $p = q$ and $\theta = 0$. In the calculation of Eq.(9), simply apply the quadrature of interior grids that excludes the point $\xi = 1$ (i.e., $\theta = 0$) will bypass the trouble of the singularity [18]. The eigenvalue equation becomes

$$\left(\frac{p^2}{2} - E\right) \chi_{nl}(p) + 4\pi p \int q dq [a_l(p, q) + b_l(p, q)] \chi_{nl}(q) = 0. \quad (11)$$

In the calculation, the denser grids in small value than in large value will be advantageous numerically. A good choice is the nonlinear mapping $p(x) = L \frac{1+x+\beta}{1-x+\alpha}$, where $x \in (-1, +1)$ and L, α, β are adjustable parameters that are not sensitive to the results. We use the Chebyshev grids, $\{x_1, x_2, \dots, x_N\}$, where $\{x_i\}$ are roots of the Chebyshev polynomial $T_N(x)$, and weight $W_t = \pi/N$. With the grids $\{x_i\}$, the quadrature rule is given by

$$\int \frac{F(x)}{\sqrt{1-x^2}} dx \approx W_t \sum_{i=1}^N F(x_i). \quad (12)$$

For the hydrogen atom, the eigenvalue equation becomes

$$\sum_{j=1}^N \left\{ \left(\frac{p_i^2}{2} - E\right) \delta_{i,j} + 4\pi p_i p_j [a_l(p_i, p_j) + b_l(p_i, p_j)] p'_j W_t \right\} \chi_{nl}(p_j) = 0, \quad (13)$$

where $p'(x_j) \equiv p'_j = \frac{dp(x)}{dx}|_{x=x_j}$. Let

$$\chi_{nl}(p) = \frac{u_{nl}(x)}{\sqrt{p'(x)}}, \quad (14)$$

and expand $u_{nl}(x)$ in terms of the cardinal function $g_j(x)$,

$$u_{nl}(x) \approx \sum_{j=1}^N u_{nl}(x_j) g_j(x), \quad (15)$$

where the cardinal function is [19]

$$g_j(x) = \frac{T_N(x)}{T'_N(x_j)}[x - x_j]^{-1}, \quad (16)$$

and $g_j(x_k) = \delta_{j,k}$. The eigenvalue equation becomes

$$\sum_{j=1}^N \left\{ \left(\frac{p_i^2}{2} - E \right) \delta_{i,j} + 4\pi p_i p_j \sqrt{p'_i p'_j} [a_l(p_i, p_j) + b_l(p_i, p_j)] W_t \right\} u_{nl}(x_j) = 0. \quad (17)$$

The matrix eigenvalue problem is real-symmetric. A solver is available from LAPACK [20].

III. METHOD OF THE TIME-DEPENDENT SCHRÖDINGER EQUATION

To demonstrate an application of the generated eigenset, we describe the method to solve the time-dependent Schrödinger equation (TDSE) for a hydrogen atom under the interaction of a linearly polarized pulse. The method for other SAE atom is similar. There are several available packages in R -space for calibration [23, 24]. Let the electric field and vector potential be

$$\vec{E}(t) = \hat{z} E_m \sin^2\left(\frac{\pi t}{T}\right) \cos(\omega t + \phi) \equiv \hat{z} E(t), \quad t \in [0, T], \quad (18)$$

$$\vec{A}(t) = -\hat{z} \int_0^t E(t') dt', \quad (19)$$

where E_m is the peak electric field amplitude, E_m^2 is the peak intensity, ϕ is the carrier-envelope phase, ω is the laser frequency and T is the pulse duration. The time-dependent interaction hamiltonian can be written as

$$H'(t) = A(t)p_z. \quad (20)$$

The split-operator-algorithm for wavepacket time evolution is

$$|\Psi(t + \Delta)\rangle = e^{-iH_0 \frac{\Delta}{2}} e^{-iH'(t')\Delta} e^{-iH_0 \frac{\Delta}{2}} |\Psi(t)\rangle + O(\Delta^3), \quad \text{with} \quad (21)$$

$$t' = t + \frac{\Delta}{2}.$$

The time marching scheme for t to $t + \Delta$ contains the following steps :

A. $|\Psi_1(t)\rangle \equiv e^{-iH_0 \frac{\Delta}{2}} |\Psi(t)\rangle$

Let

$$\Psi(p, \Omega; t) \equiv \sum_{l=0}^{L_m} f_{lm}(p; t) Y_{lm}(\Omega) / p, \quad (22)$$

where the initial magnetic quantum number m is conserved under linearly polarized pulse, and angular momenta from $l = 0$ to $l = L_m$ being used,

$$\begin{aligned}
|\Psi_1(t)\rangle &\equiv e^{-iH_0\frac{\Delta}{2}}|\Psi(t)\rangle, \\
&= \sum_{n,l} e^{-iH_0\frac{\Delta}{2}}|nlm\rangle\langle nlm|\Psi(t)\rangle, \\
&= \sum_{n,l} e^{-iE_{nl}\frac{\Delta}{2}}|nlm\rangle \int dqdq\Omega\chi_{nl}^*(q)Y_{lm}^*(\Omega)\Psi(q,\Omega;t), \text{ with} \\
\Psi_1(p,\Omega;t) &\equiv \sum_{l=0}^{L_m} f_{lm}^{(1)}(p;t)Y_{lm}(\Omega)/p, \text{ then} \tag{23}
\end{aligned}$$

$$f_{lm}^{(1)}(p;t) = \sum_n e^{-iE_{nl}\frac{\Delta}{2}}\chi_{nl}(p) \int dq\chi_{nl}^*(q)f_{lm}(q;t). \tag{24}$$

Using the Gauss-Chebyshev quadrature, we have

$$\begin{aligned}
f_{lm}^{(1)}(p_j;t) &= \sum_k A_{j,k}^{(l)}f_{lm}(p_k;t), \\
A_{j,k}^{(l)} &= \sum_n e^{-iE_{nl}\frac{\Delta}{2}}\chi_{nl}(p_j)\chi_{nl}^*(p_k)p'_k W_t. \tag{25}
\end{aligned}$$

The matrix $A^{(l)}$ for each (l, m) is time-independent and is m-independent, $l \in [0, L_m]$ with the maximum angular momentum L_m . It can be constructed outside of the time marching loop.

$$\mathbf{B.} \quad |\Psi_2(t)\rangle \equiv e^{-iA(t+\frac{\Delta}{2})p \cos \vartheta \Delta} |\Psi_1(t)\rangle$$

Let's write

$$\Psi_2(p,\Omega;t) \equiv \sum_{l=0}^{L_m} f_{lm}^{(2)}(p;t)Y_{lm}(\Omega)/p. \tag{26}$$

By using the Rayleigh's formula

$$e^{-iA(t')p \cos \vartheta \Delta} = \sum_{k=0} (-i)^k (2k+1) j_k[A(t')p\Delta] P_k(\cos \vartheta), \tag{27}$$

where $t' = t + \frac{\Delta}{2}$, j_k is the spherical Bessel function and P_k is the Legendre polynomial; especially for the case of $m = 0$, we can derive

$$f_{l_0}^{(2)}(p;t) = \sum_{l_1, l_2} (-i)^{l_1} j_{l_1}[A(t')p\Delta] (2l_1+1) \sqrt{(2l+1)(2l_2+1)} f_{l_2 0}^{(1)}(p;t) \begin{pmatrix} l & l_1 & l_2 \\ 0 & 0 & 0 \end{pmatrix}^2, \tag{28}$$

where the last symbol in the above equation is square of a Wigner-3j symbol.

C. $|\Psi(t + \Delta)\rangle \equiv e^{-iH_0 \frac{\Delta}{2}} |\Psi_2(t)\rangle$

This step repeats the algorithm of step A.

D. Above-threshold-ionization and photoelectron angular distribution

At the end of pulse, we write the final wave function as

$$\Psi(t = T) \equiv \Psi_f(\vec{p}) = \sum_l f_{lm}(p; T) Y_{lm}(\Omega)/p. \quad (29)$$

For the above-threshold-ionization (ATI) and photoelectron angular distribution (PAD), we need the wave packet $\Psi^{conti}(\vec{p})$ in the continuum,

$$\Psi^{conti}(\vec{p}) = \Psi_f(\vec{p}) - \sum_{nlm} \Psi_{nlm}^{bound}(\vec{p}) \int \Psi_{nlm}^{bound}(\vec{q})^* \Psi_f(\vec{q}) d^3q, \quad (30)$$

$$\equiv \sum_l g_{lm}(p) Y_{lm}(\Omega)/p, \quad (31)$$

$$g_{lm}(p) = f_{lm}(p) - \sum_n \chi_{nl}^{bound}(p) \int dq \chi_{nl}^{bound}(q)^* f_{lm}(q), \quad (32)$$

where $\chi_{nl}^{bound}(p)$ are radial wave function of bound state with quantum number (nl). Let the ionization probability be \mathcal{P} , then

$$\begin{aligned} \mathcal{P} &\equiv \int_{\epsilon=0}^{\infty} \frac{\partial \mathcal{P}}{\partial \epsilon} d\epsilon = \int |\Psi^{conti}(\vec{p})|^2 d^3p, \text{ where} \\ \frac{\partial \mathcal{P}}{\partial \epsilon} &= \int \int p |\Psi^{conti}(\vec{p})|^2 d\Omega \\ &= \sum_l |g_{lm}(p)|^2 / p. \end{aligned} \quad (33)$$

The photoelectron angular distribution (PAD) is conveniently expressed in 2-dimensional momentum plot. Let p_{\parallel} and p_{\perp} be the component of momentum \vec{p} in parallel and in perpendicular to the polarization axis, ϑ be the angle between \vec{p} and the polarization axis, then $p_{\parallel} = p \cos \vartheta$, and $p_{\perp} = \sqrt{p_x^2 + p_y^2} = p \sin \vartheta$. The ionization probability \mathcal{P} will be expressed as

$$\begin{aligned} \mathcal{P} &\equiv \int \frac{\partial^2 \mathcal{P}}{\partial p_{\parallel} \partial p_{\perp}} dp_{\parallel} dp_{\perp}, \text{ where} \\ \frac{\partial^2 \mathcal{P}}{\partial p_{\parallel} \partial p_{\perp}} &= \int p_{\perp} \cdot |\Psi^{conti}(\vec{p}, t = \infty)|^2 d\varphi. \end{aligned} \quad (34)$$

IV. RESULTS AND DISCUSSIONS

We apply the present momentum space method to the hydrogen atom first. The results can be compared to the exact solutions. Some low-lying hydrogen radial wave functions $F_{nl}(p) \equiv \chi_{nl}(p)/p$ were listed in Ref.[11]. Those bound state $F_{nl}(p)$ which are not listed can be derived by using the Gegenbauer polynomials. The exact energy level $E(nl)_{exact}$ of eigenstate $\Phi_{nlm}(\vec{p})$ is equal to $-1/(2n^2)$. We showed the error for calculated energy level $\Delta E = |E(nl) - E(nl)_{exact}|$ to demonstrate the accuracy. In Table I, we listed the accuracy of some calculated hydrogen low-lying energy levels. The tabulated results are of 512 and 1024 grid numbers with momentum maximum $p_{max} = 50$. For the $N=512$ case, the relative errors are in order of $10^{-10} \sim 10^{-4}$. The worst one is the ground state with error 3.46×10^{-4} which is correct up to the fourth place after the decimal point. For $N = 1024$, it is accurate up to the sixth decimal place. Because the ground state wave function $F_{1s}(p) = \sqrt{\frac{32}{\pi}} \frac{1}{(1+p^2)^2}$ decays slowly with p , a larger p_{max} can give higher accuracy. Other excited state wave function is located in a small region of p such that $p_{max} = 50$ gave good accuracy. Doubling the grid number, the accuracy improves in nearly two orders of magnitude. Compared with $N = 2048$, $p_{max} = 100$ of case I, Table I in Ref.[15] of our previous complicated Lande subtraction method, the present accuracy with half grid number has been competitive or even better. The results show that high accuracy in $E(nl)$ was reached at a modest number of grids.

For the accuracy of calculated wave functions, we use the root-mean-square (rms) deviation for $\chi_{nl}(p)$,

$$\Delta\chi_{nl} = \sqrt{\frac{1}{N} \int dp [\chi_{nl}(p) - \chi_{nl}(p)_{exact}]^2}, \quad (35)$$

where $\chi_{nl}(p)_{exact}$ are obtained through the analytical wave functions [11]. In Table II, we listed the rms deviations of the first four low-lying states for $L = 0, 1, 2, 3$. The high accurate results were shown. The rms deviation is in the order of $10^{-10} \sim 10^{-6}$ with grid number $N=1024$. Accuracy improves about two orders by increase $N=512$ to 1024. Again, the accuracy is competitive or even better than the Lande method. The rms deviation represents typical deviation of wave function at each grid point. This accuracy is good enough for the further applications such as time-dependent calculations. In Table III, we tabulated errors of the first four low-lying energy levels of $L = 0, 1, 2, 3$ for helium with SAE potential. We use the results generated by the high accurate eigenstate solver [21] for

comparison. Compare with the Case I, Table II of Ref.[15] at $N = 1024$ and $p_{max} = 50$, we can find more than two orders of improved accuracy were reached. We can claim that the excellent accuracy has been reached.

In the first TDSE check, we calculate the ground state hydrogen atom under the interaction of a 800nm, FWHM 10fs Sine-square envelope pulse in the electric field with peak intensity $1.0 \times 10^{14}W/cm^2$. The corresponding vector potential is calculated through $A(t) = -\int_{-\frac{T}{2}}^t E(t')dt'$. Fig.1a is the above-threshold-ionization (ATI) spectrum which is to compare with the Fig.10a of [22]. The shape and magnitude are totally agreed with each other. Fig.1b is the corresponding photoelectron angular distribution (PAD). PAD shows the density distribution for photoelectron with momentum in parallel and in perpendicular to the polarization direction. The depicted photoelectron kinetic energy of $0 \sim 7eV$ in Fig.1a corresponds to the electron momentum in $0 \sim 0.72 a.u.$ The first 3 peaks group in ATI corresponds to the fan structure for $0 < p < 0.4$. The next 3 ATI peaks are rings in $0.4 < p < 0.61$. The number of zero stripes in the PAD shows the corresponding angular momentum. For the first fan group, there are 3 zero stripes in PAD which the corresponding Legendre polynomial is of order 3, that is, the photoelectron angular momentum $l = 3$. In this calculation, we use $l \in [0, 31]$ of the generated eigenset with $p_{max} = 50$ at 1024 grids. The convergence is checked with L_{max} increased up to 47. In the next case, we calculate hydrogen ground state under 535nm, 20-cycle, peak intensity $2 \times 10^{13}W/cm^2$, Sine-squared envelope vector potential pulse. This is to compare with Fig.2 of [23]. In our Fig.2a, we showed the ATI. We can see the results agree well with [23]. Also showed is the corresponding PAD in Fig.2b. The PAD contains information of photoelectron detailed distribution in momentum space.

V. CONCLUSIONS

By using the simple and straightforward quadrature and nonlinear mapping in momentum grids, the accuracy of SAE low-lying states in momentum space has been competitive or better than our previous complicated Lande method [15]. In which, we improved the Lande subtraction by analytic extension of momentum range from a finite upper limit p_{max} to infinity. Much more complicated formalism is required than current method. For the ground state, its momentum space wave function vanishes slowly with p . Hence an increase of

p_{max} is helpful for better accuracy. For the excited states and continuous states, the wave functions squeezed into the small momentum region. A modest p_{max} and the denser grids near origin than in the large value of momentum are necessary for the accurate spectrum. This requirement was fulfilled by the nonlinear mapping. Changing the mapping parameter in $p = p(x)$ can adjust the grids distribution and improve the accuracy a little but not in a sensitive way. Increasing the number of grid points will improve the accuracy a lot by comparison the results of $N = 512$ and $N = 1024$. High precision is capable with a large p_{max} and increase of grid points. The data in Tables I and III showed that the errors in energy levels were quite small indeed. The rms deviation of wave function showed in Table II elucidated the good accuracy was reached. The calculation in this paper was carried out in a desktop personal computer with Intel Xeon(R) E5-2630v3 cpu. Results of Table I and II with $N = 512$ cost wall time of ~ 29 second, and the cpu time scales to $\sim N^2$. Application of the present momentum space method in the study of strong light generated photoelectron has the advantage over coordinate space method [1, 2, 15]. We showed two TDSE examples of a hydrogen atom under laser pulses. The agreements with published results are very good. This is just to demonstrate the applicability of P -space method because of calculations in this category were not general. We have developed the TDSE code in GPU. The capability of solving TDSE with circular polarized pulse has been realized. Theoretical investigation on recently interested problems such as mid-infrared pulse on atoms, low-energy structure photoelectron spectra [25], dichroism [26], spin polarization of photoelectron [27] etc. are under progress.

Acknowledgment The work is supported by the Ministry of Science and Technology, Taiwan under contract numbers MOST105-2112-M-009-003 and MOST105-2811-M-009-060.

-
- [1] Zhongyuan Zhou and Shih-I Chu, Phys. Rev. **A83**, 013405 (2011).
- [2] N.I. Shvetsov-Shilovski and E. Räsänen, J. Comp. Phys. **279**, 174 (2014).
- [3] L. Tao and A. Scrinzi, New J. Phys. **14**, 013021 (2012); A. Scrinzi, Phys. Rev. **A81**, 053485 (2010).
- [4] Toru Morishita, Z. Chen, S. Watanabe, and C.D. Lin, Phys. Rev. **A75**, 023407 see the appendix (2007).
- [5] X.M. Tong, K. Hino, and N. Toshima, Phys. Rev. **A74**, 031405R (2006); X.M. Tong, S. Watahiki, K. Hino, and N. Toshima, Phys. Rev. Lett. **99**, 093001 (2007).
- [6] B. Podolanski and L. Pauling, Phys. Rev. **34**, 109 (1929).
- [7] V.A. Fock, Z. Physik **98**, 145 (1935).
- [8] Leon A. Takhtajan, *Quantum Mechanics for Mathematicians*, Graduate Studies in mathematics, V.95 (American Mathematical Society, Providence, Rhode Island, 2000).
- [9] H.A. Bethe and E.E. Salpeter, *Quantum Mechanics of One- and Two-electron Atoms*, Sect. 8 (Plenum, New York, 1977).
- [10] S. Flügge, *Practical Quantum Mechanics*, Problem 77,78 (Springer-Verlag, New York, 1974).
- [11] B.H. Bransden and C.J. Joachain, *Physics of Atoms and Molecules*, second ed., Appendix 5 (Prentice Hall, New York, 2003).
- [12] Y.R. Kwon and F. Tabakin, Phys. Rev. **C18**, 932, cited Ref. 8 (1978).
- [13] J.W. Norbury, K.M. Maung, and D.E. Kahana, Phys. Rev. **A50**, 2075 (1994).
- [14] A. Tang and J.W. Norbury, Phys. Rev. **E63**, 066703 (2001).
- [15] Tsin-Fu Jiang, Shih-Da Jheng, Yun-Min Lee and Zheng-Yao Su, Phys. Rev. **E86**, 066702 (2012).
- [16] X.M. Tong and C.D. Lin, J. Phys. **B38**, 2593 (2005).
- [17] http://physics.nist.gov/PhysRefData/ASD/levels_form.html
- [18] T.W. Chiu, J. Math. A: Math. Gen. **19**, 2537 (1986).
- [19] John P. Boyd, "Chebyshev and Fourier Spectral Methods", Second Ed. (Dover Publications, New York, 2001).
- [20] <http://www.netlib.org/lapack/>
- [21] F. Salvat and R. Mayol, Comp. Phys. Commun. **62**, 65 (1991).

- [22] Z. Chen, Toru Morishita, Anh-Thu Le, M. Wickenhauser, X.M. Tong, and C.D. Lin, Phys. Rev. A **74**, 053405 (2006).
- [23] V. Mosert and D. Bauer, Comp. Phys. Commun. **207**, 452 (2016).
- [24] S. Patchkovskii and H.G. Muller, Comp. Phys. Commun. **199**, 153 (2016).
- [25] C. I. Blaga, F. Catoire, P. Colosimo, G. G. Paulus, H. G. Muller, P. Agostini, and L. F. DiMauro, Nature Phys. **5**, 335 (2009); Benjamin Wolter *et al.*, Phys. Rev. **X5**, 021034 (2015); Benjamin Wolter *et al.*, Phys. Rev. **A90**, 063424 (2014).
- [26] A. Ferré *et al.*, Nature Photonics **9**, 93 (2015); D. Baykusheva, M.S. Ahsan, N. Lin, and H.J. Wörner, Phys. Rev. Lett. **116**, 123001 (2016); C.A. Mancuso *et al.*, Phys. Rev. **A93**, 053406 (2016).
- [27] A. Hartung *et al.*, Nature Photonics **10**, 526 (2016); D.B. Milosević, Phys. Rev. **A93**, 051402R (2016).

TABLE I. The magnitude of errors $\Delta E(i), i = 1, 2, 3, 4$ for the hydrogen lowest four levels of $L = 0, 1, 2, 3$. ΔE is defined as $|E(nl) - E(nl)_{exact}|$, with $E(nl)_{exact} = -1/(2n^2)$ and $E(nl)$ denotes the calculated energy level. The numbers of grid points are 512,1024 respectively, and $p_{max} = 50$. 3.46E-4 designates 3.46×10^{-4} .

state and	$\Delta E(1)$		$\Delta E(2)$		$\Delta E(3)$		$\Delta E(4)$	
grid points	512	1024	512	1024	512	1024	512	1024
$L = 0$	3.46E-4	3.77E-6	5.74E-5	3.93E-7	1.80E-5	1.12E-7	7.75E-6	4.65E-8
$L = 1$	3.57E-6	1.41E-8	1.34E-6	5.04E-9	6.12E-7	2.25E-9	3.24E-7	1.18E-9
$L = 2$	2.36E-8	1.8E-11	1.46E-8	1.0E-11	8.67E-9	6.3E-12	5.41E-9	4.2E-12
$L = 3$	1.1E-10	1.5E-12	9.5E-11	6.0E-13	7.0E-11	5.4E-13	2.6E-10	2.1E-10

TABLE II. The root-mean-square deviations $\Delta\chi_{nl}(i), i = 1, 2, 3, 4$ of wave function for the hydrogen lowest four states of $L = 0, 1, 2, 3$. The numbers of grid points are 512,1024 respectively, and $p_{max} = 50$.

state and	$\Delta\chi(1)$		$\Delta\chi(2)$		$\Delta\chi(3)$		$\Delta\chi(4)$	
grid points	512	1024	512	1024	512	1024	512	1024
$L = 0$	4.49E-5	6.69E-7	4.05E-5	3.85E-7	4.02E-5	3.35E-7	4.03E-5	3.26E-7
$L = 1$	4.92E-6	3.28E-8	4.39E-6	2.40E-8	4.24E-6	2.09E-8	4.23E-6	1.98E-8
$L = 2$	3.18E-7	2.62E-9	2.67E-7	3.06E-9	2.24E-7	3.33E-9	1.98E-7	3.57E-9
$L = 3$	4.51E-8	5.2E-11	5.73E-8	6.4E-11	6.54E-8	7.1E-11	7.39E-8	9.4E-10

TABLE III. The magnitude of errors $\Delta E(i), i = 1, 2, 3, 4$ for the SAE Helium lowest four levels of $L = 0, 1, 2, 3$. ΔE is defined as $|E(nl) - E(nl)_R|$ where $E(nl)_R$ is the level accurately calculated by the solver of Ref.[21] and $E(nl)$ denotes the calculated energy level by current momentum space method. The numbers of grid points are 512,1024 respectively, and $p_{max} = 100$.

state and grid points	$\Delta E(1)$		$\Delta E(2)$		$\Delta E(3)$		$\Delta E(4)$	
	512	1024	512	1024	512	1024	512	1024
$L = 0$	1.54E-3	8.40E-5	1.70E-4	6.92E-6	4.66E-5	1.81E-6	1.89E-5	7.22E-7
$L = 1$	9.30E-6	1.03E-7	3.37E-6	3.59E-8	1.52E-6	1.57E-8	8.02E-7	8.16E-9
$L = 2$	4.44E-8	3.7E-10	2.69E-8	9.0E-11	1.59E-8	4.2E-11	9.92E-9	2.0E-11
$L = 3$	4.4E-10	2.5E-10	3.0E-10	1.3E-10	1.9E-10	7.1E-11	1.3E-10	4.2E-11

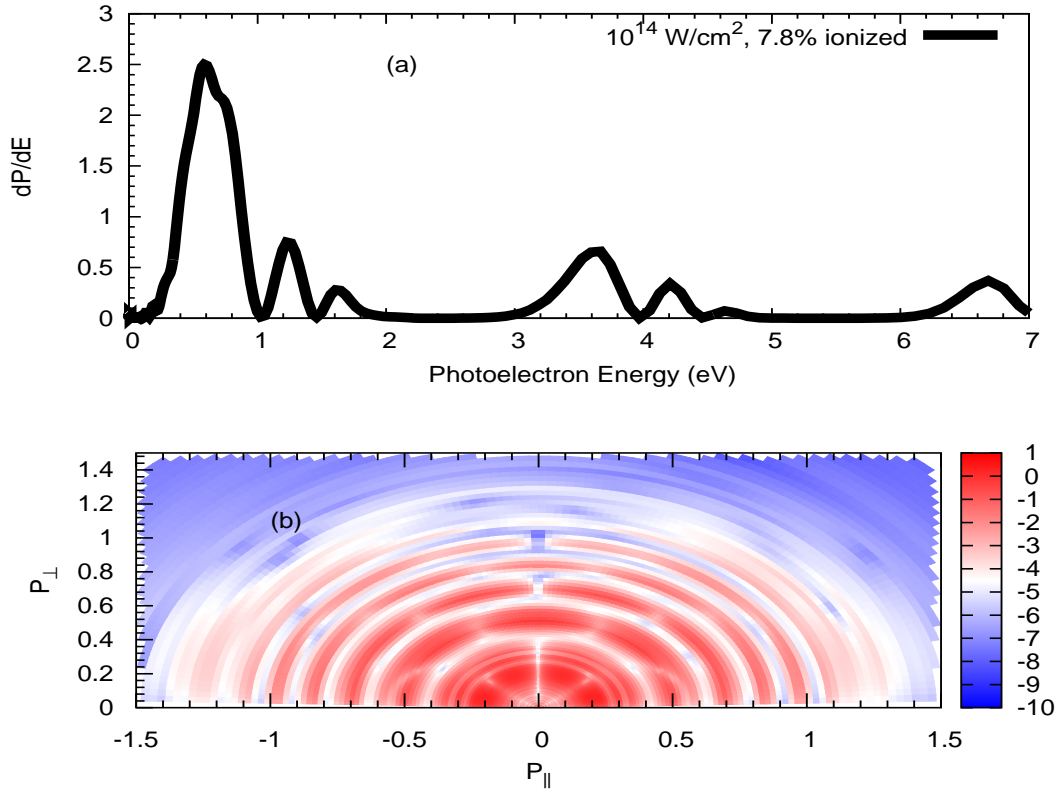


FIG. 1. (Color online) (a) The ATI spectrum of the hydrogen atom under the interaction of a 800nm, FWHM $10fs$ Sine-square envelope pulse in the electric field with peak intensity $1.0 \times 10^{14}W/cm^2$. The plot is to compare with Fig.10a of Ref.[22]. (b) The corresponding PAD.

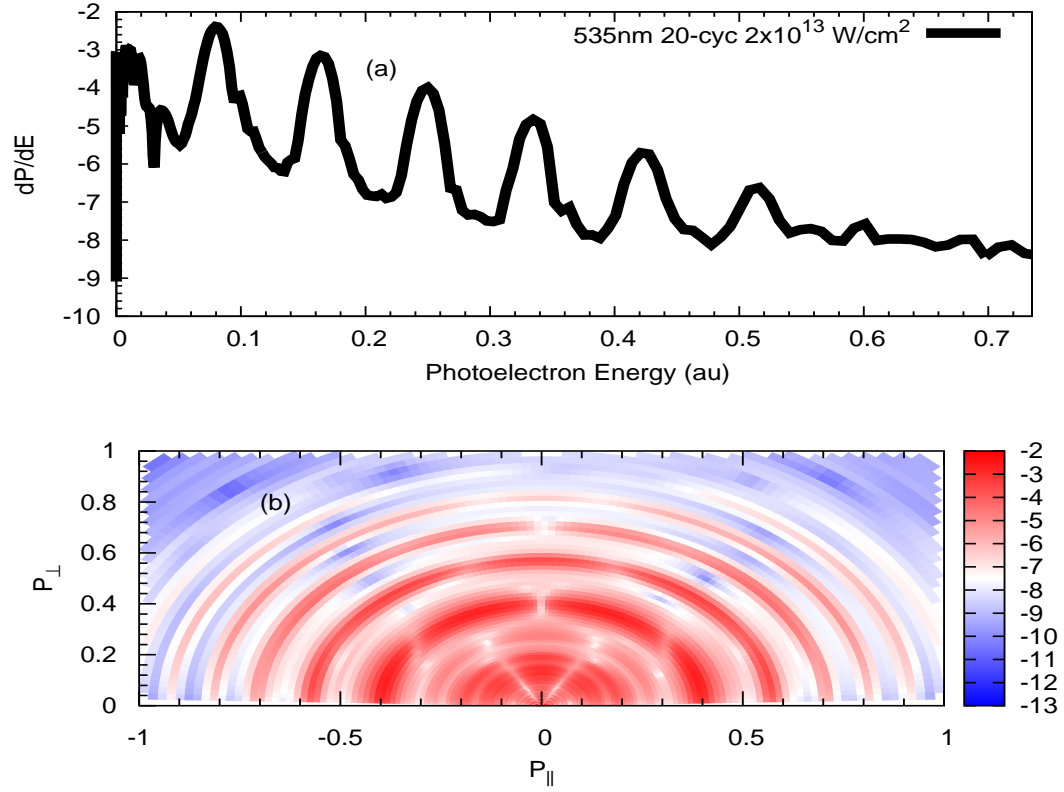


FIG. 2. (Color online) (a) The hydrogen atom under 535nm, 20-cycle, peak intensity $2 \times 10^{13} \text{ W/cm}^2$, Sine-squared envelope pulse in vector potential. This is to compare with Fig.2 of [23]. The vertical axis is in exponential scale. (b) The corresponding PAD.